
Check for updates

...charges (*e.g.*, screening clouds), and polar-

...prism is oriented along the y axis, then the holo-... ideal imaging system can be expressed in the form

$$\left|\psi\left(x-\frac{d}{2},y\right)\exp\left(\frac{i\pi x}{s}\right)+\psi\left(x+\frac{d}{2},y\right)\exp\left(-\frac{i\pi x}{s}\right)\right|^2, \tag{2}$$

...e interference distance (which depends on the biprism ...nd s is the spacing of the interference fringes in a vacuum ...ologram recorded with the specimen removed from the field ...OV). Eq. (2) describes two twin images of the object wave-

...e object (specimen) is located at $x + d/2$, then the corre-...ng object wave $\psi\left(x+\frac{d}{2},y\right)$ is overlapped with the reference ... $\psi\left(x-\frac{d}{2},y\right)$. In order to retrieve the amplitude and phase of the ...ect wave, the reference wave should ideally be equal to unity, or it ...ould be known.

When long-range electrostatic fields originate from the specimen, as shown in Fig. 1, the reference wave may be perturbed. Analysis of the hologram then results in the reconstruction of a fictitious specimen, which can be described by the wavefunction [8,9]

$$\psi(x,y)=a(x,y)\exp\left[i\varphi\left(x+\frac{d}{2},y\right)-i\varphi\left(x-\frac{d}{2},y\right)\right], \tag{3}$$

where $a(x, y)$ is the amplitude of the object wave, d is a two-dimensional "interference distance" vector that connects the two virtual sources created by the biprism, and $\varphi\left(x+\frac{d}{2},y\right)$ and $\varphi\left(x-\frac{d}{2},y\right)$ are the phases of the object and reference waves, respectively. The difference between these two phase distributions, rather than the true object phase, is then recovered. The influence of such a perturbed reference wave (PRW) on measurements of charge density and electric field is

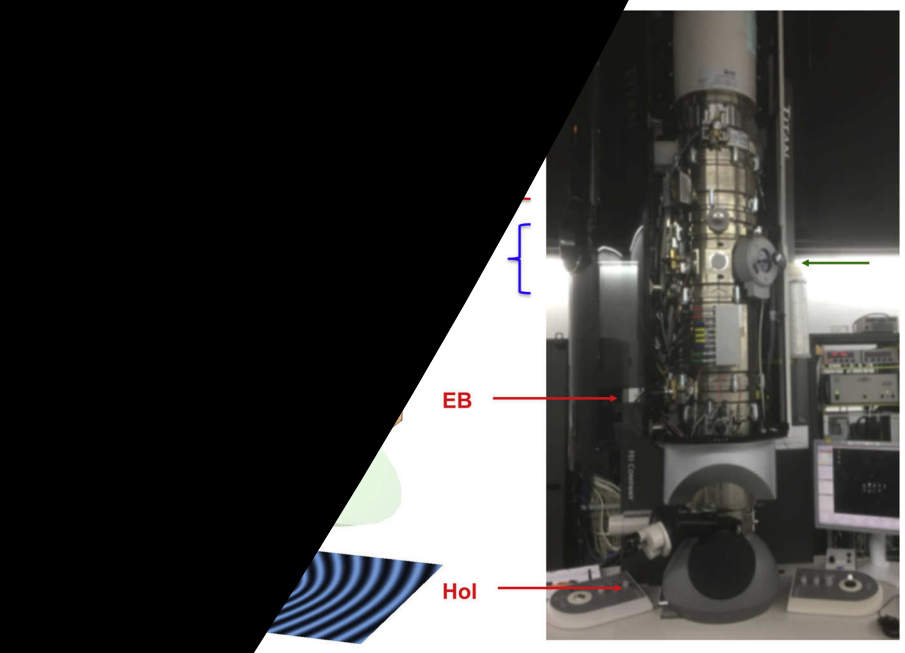

Fig. 1. Schematic diagram of the experimental setup for off-axis electron holography (left) and photograph of an FEI Titan transmission electron microscope in Forschungszentrum Jülich (right). Corresponding components are labelled using the same colours. From top to bottom are: an illuminating plane or spherical electron wave *I*, an electrically-biased needle-shaped specimen *Sp*, the electron microscope objective lens *OL*, an electron biprism *EB*, and a recorded off-axis electron hologram *Hol*.

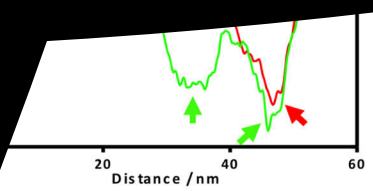

needle-shaped W specimen covered by an amorphous layer: (a) holography. (b) Charge density distribution calculated from the n the vacuum side of the specimen edge, while an effective band of ls of charge are present at the interface between the needle and the Laplacian of the phase across regions A (green) and B (red) marked in applied to a median-filtered version of the phase. See text for details.

tor, $\rho_{\mathrm{proj}}(x, y) = \int \rho\left(x - \frac{d}{2}, y, z\right) dz$ is the projected charge den- and Q_C is the total charge present in region C. The volume over ich Gauss' law is evaluated, as discussed above, is an infinite cylinder long the z axis), of which C is a cross-section.

Furthermore, the Laplacian of the phase can be calculated directly from the reconstructed complex wavefunction using the expression [25]

$$\nabla^2\varphi = \mathrm{Im}\left[\frac{\nabla^2\psi}{\psi} - \left(\frac{\nabla\psi}{\psi}\right)^2\right]. \tag{8}$$

By making use of the divergence theorem, Eq. (7) can equivalently be written in the form [17]

$$Q_C = -\frac{\epsilon_0}{C_E}\oint_{\partial C} \nabla\varphi_{\mathrm{rec}}(x(l), y(l))\cdot\mathbf{n}(x(l), y(l))\,\mathrm{d}l, \tag{9}$$

where ∇ is a two-dimensional gradient operator, ∂C denotes an integration loop (coinciding with the boundary of the integration region C in Eq. (7)), l is a curvilinear coordinate along the contour and $\mathbf{n}$ is the outward normal to the contour.

2.2. Practical considerations

Parameters that can affect charge density measurements include the MIP contribution to the phase, the spatial resolution (*i.e.*, the digital undersampling) of the recorded phase image, its signal-to-noise ratio (SNR), strong diffraction conditions (which can affect the measurement of the MIP contribution to the phase), electron-beam-induced specimen charging effects and the influence of sample imperfections (*e.g.*, damage, contamination, and oxidation). Several of these considerations are now discussed.

2.2.1. Mean inner potential

The MIP of the specimen affects charge density measurements from electron optical phase images because it is associated with the presence of effective local dipole layers at the specimen surface [42]. Its influence is illustrated in Fig. 2. Fig. 2a shows part of a phase image of the end of an unbiased W needle recorded using off-axis electron holography. The needle is surrounded at its end by a layer of amorphous oxide and/or contamination. Fig. 2b shows the projected charge density distribution calculated directly from the Laplacian of the recorded phase image using Eq. (7). Evaluation of the Laplacian of the phase invariably results in a noisy image. In addition, Fig. 2b reveals that local variations in specimen thickness and MIP are visible in the form of

phase information about a spe-

ratio

charge measurement is determined by factors that he original hologram, the sampling density of the the size of the integration region in the loop integral experimental phase image (neglecting scattering ab- specimen) is considered to be a superposition of a noise- ase image and random normally-distributed noise with nd standard deviation (SD) $\delta\varphi$, then the Laplacian of the e can also be regarded as a noise-free charge distribution . Here, we show how the SD of the measured charge density on $\delta\sigma$ is related to the SD of the phase.

iscrete Laplacian is a one-step matrix algebra operator naps each pixel in a phase image $\varphi(i, j)$ onto the value $1, j) + \varphi(i-1, j) + \varphi(i, j+1) + \varphi(i, j-1) - 4\varphi(i, j)$. If this ration is applied to a noisy phase image that has zero mean and $\delta\varphi(i, j)$, then the result is another noisy image, which is lso normally distributed and has zero mean (because $1 + 1 + 1 + 1 - 4 = 0$), but which has a standard deviation that is $\sqrt{20}$ times larger than the SD of the original image. This description is valid when each noise pixel is uncorrelated with its neighbours and when the SDs can be added in quadrature, such that $1^2 + 1^2 + 1^2 + 1^2 + 4^2 = 20$. The relationship between the SDs of the phase and the charge density is given by the expression

$$\delta\sigma = \sqrt{20}\,\frac{\epsilon_0}{C_E}\frac{\delta\varphi}{p^2} = \sqrt{20}\,\frac{\delta q}{p^2}, \tag{10}$$

where p is the pixel size, and we define $\delta q = \frac{\epsilon_0}{C_E}\delta\varphi$ as the charge noise. For reference, $\delta\varphi = 118$ mrad corresponds to $\delta q = 1e$ at 300 kV. Since experimental values of phase noise SD are typically well below 100 mrad, the achievement of single electron sensitivity in charge measurement appears to be relatively straightforward.

Eq. (10) is derived on the assumption of uncorrelated/white noise in the phase image. However, this situation does not strictly hold for Fourier-transform-based hologram reconstruction, as noise correlations are automatically introduced when a side-band is masked using an aperture. (A general description of the introduction of correlation in the reconstruction of holograms can be found elsewhere [44].) Such a mask may be "soft" (*e.g.*, Gaussian, Hann, or Butterworth), or "hard" (*e.g.*, top hat). Soft apertures are most commonly used because they are more efficient than hard apertures at suppressing phase noise without

at
els,
ks or
e and
he MIP
mulative
ase images
ndary of the
ages, often to
ing the charge

ion (see Section 2.1),
s determined by the size
of the hologram, which
age, in addition to damping

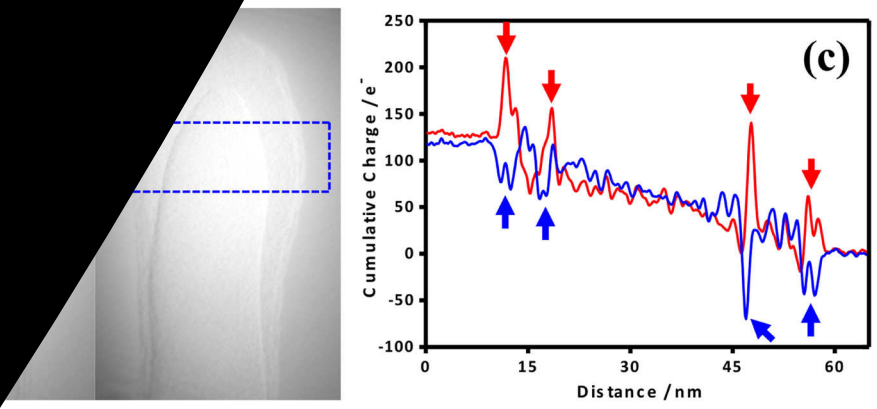

Fig. 3. Charge density distributions calculated by applying a loop integral (evaluated using Eq. (9)) to differences between phase images recorded with and without an electrical bias voltage applied to the W needle shown in Fig. 2. The phase image recorded with a bias voltage applied to the needle was deliberately misaligned by +5 and −5 pixels along the x axis in (a) and (b), respectively, with respect to the phase image recorded without an applied bias, before evaluating their difference. (c) Cumulative charge profiles obtained by integrating the signal across the regions marked in (a) and (b).

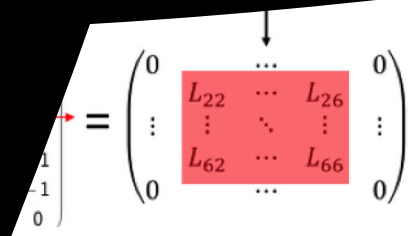

g simulated correlation matrices. (c) Experimental noise image, grams. (d) Corresponding experimental correlation matrix. Right:)

ental correlation matrix shown in Fig. 4d. The relevant correcoefficients can be extracted from the experimental correlation x shown in Fig. 4d, resulting in values of $c_1 = 0.859$, $c_{11} = 0.746$ $c_2 = 0.532$. (c_{11} was estimated by applying second-order polymial interpolation to $c_0 = 1$, c_1 and c_2). For these values, the noise ansfer factor drops from $\sqrt{20} = 4.47$ to $\sqrt{0.613} = 0.783$. As a result, the SD of the charge density calculated using Eq. (10) drops from 0.64 e/p^2 to 0.11 e/p^2, in agreement with the experimental value of the charge density noise being 0.10 e/p^2.

Integration of the measured charge density distribution reduces noise, although it does not bring it back to the value that it had in the original phase image, both because the integration region is usually smaller than the FOV and as a result of noise correlations. (Even if the phase noise were uncorrelated, the charge density noise becomes correlated as a result of the use of the discrete Laplacian operator.) The right half of Fig. 4 illustrates how the SD of the measured charge δQ is related to $\delta\sigma$ and $\delta\varphi$. We consider a simple square 7×7 matrix with noisy pixels $\delta\varphi$ representing the region of the phase image where we attempt charge measurement. The discrete Laplacian of this matrix, which is represented by a standard 3×3 kernel, is an edge-padded 5×5 matrix (the evaluation of boundary pixels is neglected for simplicity), in which each pixel value L_{ij} is a linear combination of the original pixel values written above (*e.g.*, $L_{44} = \delta\varphi_{34} + \delta\varphi_{35} + \delta\varphi_{43} + \delta\varphi_{45} - 4\delta\varphi_{44}$, *etc.*). Summing these 25 pixels gives another linear combination of pixel values. Isolating the coefficients of each pixel contributing to the sum and assembling them into a matrix yields what is shown in Fig. 4 at the end of the process diagram, which coincides with the discrete representation of the loop integral of the gradient (represented by the $(-1, 1)$ kernel) of the original image over the boundary of the chosen region. In addition to providing visual verification of the equivalence of the two methods for measuring Q, it implies that δQ is also identical. Counting the number of pixels that contribute to the measurement of Q and summing them in quadrature (for uncorrelated phase noise) provides the following relationship between the measurement uncertainty and the phase noise SD:

$$\delta Q = \sqrt{8n}\,\frac{\epsilon_0}{C_E}\delta\varphi = \sqrt{\frac{2L}{p}}\,\delta q, \tag{11}$$

where $n \gg 1$ is the number of pixels on one side of the square integration loop and L is the total length of the loop. The noise transfer factor in the case of correlated phase noise becomes $\sqrt{8(1 - c_1)n}$, where the only relevant correlations are those between adjacent pixels in the Laplacian. Since these correlations are also the strongest, c_1 can

…to have accumulated at the edges
…e in the presence of the applied voltage of 50 V.
…mulative charge profile in the specimen (blue)
…rating the charge density in Fig. 7a parallel to the
…he approach described in Section 2.1. The integra-
…ed by a red dashed rectangle in Fig. 7a. The charge in
…egative. The approximately constant slope of the cu-
… profile suggests that the charge density in each slice of
…nsional volume of the specimen is the same, *i.e.*, that it
…imately constant linear charge density parallel to its axis.

…*ical model-dependent reconstruction*

…nalytical model-dependent approach for determining the
…density from an electron optical phase image relies on having
… to a model that can be used to solve the Laplacian equation. A
…e-shaped specimen has often been modelled as a line charge in
…t of a grounded conducting plane. The justification for using such a
…del is that equipotential surfaces around a line of constant charge
…ensity take the form of ellipsoids, which are in turn similar to the outer
…boundary of a needle-shaped specimen, which is often conducting and
expected to be an equipotential. The charge density in such a model can
be adjusted until a best match is found between experimental and si-
mulated phase images in vacuum outside the specimen. The influence
of the grounded conducting plane on the electrostatic potential dis-
tribution and its electron optical phase can be included by using image
charge methods [22]. In the presence of an external field, a linear
charge density that increases along the length of the needle can be used
in the model instead of a constant charge density [23,46]. An analytical
model for the electron optical phase [23] then takes the form

$$\varphi(x, y) = \frac{KC_E}{4\pi\epsilon_0}\left[4Ly + 4xy \arctan\frac{y-L}{x} - 4xy \arctan\frac{y+L}{x} - (L^2 + x^2 - y^2)\ln\frac{x^2 + (y-L)^2}{x^2 + (y+L)^2}\right] \quad (12)$$

In the present example, the shape of the needle was fitted to an ellipsoid of major semi-axis $a = 45$ µm and minor semi-axis $b = 0.6$ µm. The value of K in Eq. (12) was found from a best fit to the phase image. Fig. 8a shows a simulated contoured phase image corresponding to the best-fitting result, with $K = 35$ e/µm^2. The electric field strength E induced by the counter-electrode and the base on which the field emitter sits can be calculated [23,46] and is approximately 0.4 MV/m, which is comparable to the electric field generated when 50 V is applied between two plates with a separation of 50 µm. Fig. 8b shows a stream plot of the electric field lines in the $z = 0$ plane for the best-fitting parameters. The maximum electric field strength at the apex E_{apex} is approximately 3.6 GV/m. The ratio E_{apex}/E corresponds to a field enhancement factor of 9000.

This field emitter was also transferred to a dedicated ultra-high-vacuum chamber to measure its field emission properties [48]. The electric field at the apex determined from a measured I–V curve was 2.2 GV/m, which is slightly lower than that determined here. However, we did not detect a field emission current during our experiment, most likely due to the poorer vacuum level in the TEM column.

4. Numerical iterative model-based reconstruction

The accuracy of the analytical model-dependent approach described

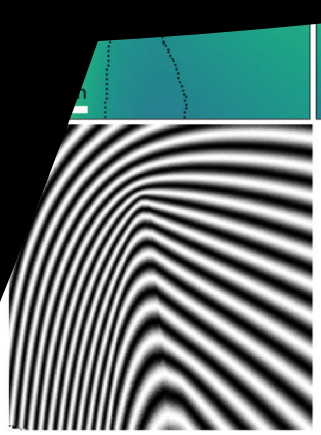

ology, corresponding to: (a) the MIP contribution alone; (b) the MIP
b) and (c), *i.e.*, the effect of the electrical bias voltage alone. The outline of
g phase contour maps, displayed in the form of the cosine of the phase. The

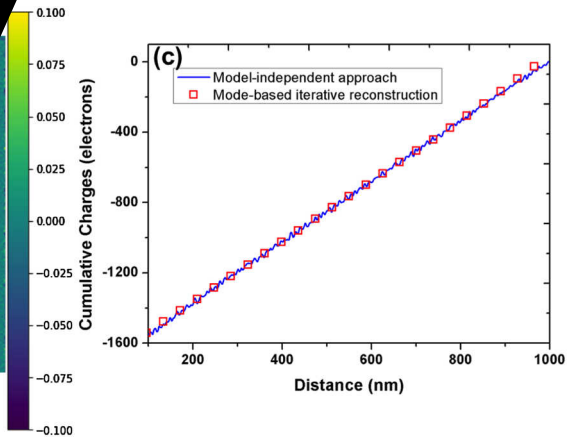

scribed in the text to measure the charge density distribution in a LaB_6 field emitter that has an electrical
density distribution determined directly from the Laplacian of the phase; (b) Charge density distribution
viation of 5 pixels (4.2 nm). (a) and (b) are both shown in units of e/pixel; (c) Cumulative charge profiles
e line) and model-based iterative reconstruction (red squares; see Section 4.4.6). The integration region is

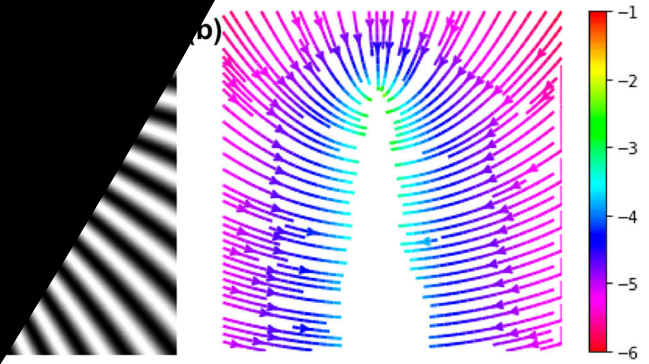

Fig. 8. Demonstration of the application of the analytical model-dependent approach described in the text to a LaB_6 field emitter that was electrically biased at 50 V. (a) Contoured phase image that provided a best fit in the vacuum region around the specimen to the experimental phase images shown in Fig. 6b and c. The phase contour spacing is 2π radians. (b) Streamlines showing a section through the electric field lines in the $z = 0$ plane calculated from the best-fitting parameters. The colour scale indicates the natural logarithm of the electric field strength. The shadow of the needle is indicated by the white region.

$+ (y - y_0')^2 + z^2}\Big)$. (16)

potential in the z direction from $+\infty$ to $-\infty$ then ssion

$$\ln \frac{(x - x_0')^2 + (y - y_0')^2}{(x - x_0)^2 + (y - y_0)^2}. \quad (17)$$

be aware that two singularities are present in the above re, we tackle this problem by treating a single voxel as a harged sphere. (See Appendix.) Fig. 10 shows a simulated p and a corresponding phase image of a dipole, in which the e separated by a distance of 32 nm.

aking use of Eq. (17), the forward model can be divided into a on of a charge density distribution in the electron beam direc- nd a subsequent phase mapping operation described by a con- ion. In discretised form, the projection and convolution can be cuted in two steps, which can be described in matrix form by the pression

$$\mathbf{y} = \mathbf{Fx} = \mathbf{MPx}, \quad (18)$$

where the matrix **F** is split into a projection matrix **P** and a convolution matrix **M**, **x** is the charge state vector (*i.e*, `q(x, y, z)` in vectorised form) and **y** describes the calculated phase images in vectorised form. An efficient implementation of the projection step can be achieved by employing sparse matrix calculations, especially in the case of projections along z axis. In order to optimise the second step, the convolution kernels (see Eq. (17)) can be pre-calculated in real space and fast convolutions can be used in Fourier space [49,51].

4.3. Regularisator

Regularisation provides a way of making use of *a priori* information in the model-based inverse algorithm. The following regularisators were used here: the application of a mask to indicate the region that can contain charges (*i.e.*, the location of the specimen); the application of a confidence mask to define trustworthy regions in the experimental phase; and the enforcement of physical or mathematical constraints by adding a Tikhonov regularisator [52] in the cost function.

The total electrostatic potential energy W of all of the charges can be written in the form [53]

$$W = \frac{1}{8\pi\epsilon_0} \sum_i \sum_j \frac{q_i q_j}{|\mathbf{r_i} - \mathbf{r_j}|}, \quad (19)$$

where q_i, q_j and $\mathbf{r_i}$, $\mathbf{r_j}$ are the magnitudes and positions of the i, jth charges, respectively. The charges interact with each other through the Coulomb force, turning a linear term (Eq. (15)) into a non-linear one. For an ideal metal, in which charges are located only on the specimen surface, Eq. (19) can be reduced to the form

$$w = \frac{\epsilon_0}{2}\sigma^2, \quad (20)$$

where w is the energy density and σ is the surface charge density. Minimisation of the total potential energy is a physical constraint that can be used to restrict the reconstruction of the charges. In order to enforce this constraint, we use Tikhonov regularisation of 0th order, which corresponds to the use of a scaled identity matrix in the regularisation term. The regularisation term is then exactly Eq. (15), *i.e.*, a Euclidean norm. Although, in general, charges do not need to be

y the as a volves es (φ or ue to the licating an at all [50]). n the form of rantees the ex-

(14)

incorporate *a priori* atical or physical con- gularisation term

(15)

Tikhonov regularisator. The nes its weight in comparison to ich favours compliance with the

nstruction process is illustrated in Fig. 9. workflow, which is used to map a chosen on onto a corresponding electrostatic phase asis for iterative reconstruction of the charge d easy model that can be incorporated in the

tities of charge density ***x*** and phase ***y*** should not be con- coordinates (x, y).

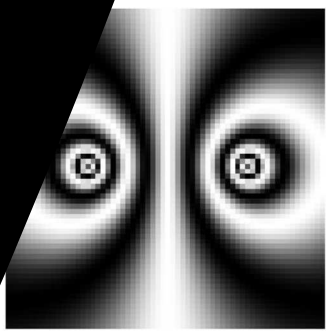

lculated for a positive charge and its image charge separated by a distance of

4.4.1. Mask

A mask can be used to specify *a priori* information about the specimen geometry, *i.e.*, the positions at which charges can be located. It can therefore lead to a significant reduction in the number of unknowns and to an improvement in the quality of the reconstruction. Although masking could be implemented as a term in the cost function, here we apply a mask by excluding these regions from the charge state vector $\mathbf{x}$, which corresponds to assuming a charge of zero in these regions. The algorithm then does not fit the regions outside the mask. Differences between input and reconstructed projected charge density distributions obtained from the phase image shown in Fig. 12, both with and without using a mask, are shown in Fig. 13. When a mask is not used, the error in the reconstructed charge is approximately 10%, while that in the phase is more than 150 μrad (not shown). There are also ripple-like artefacts in the reconstructed charge density. In contrast, when a mask (marked by the dashed circle in Fig. 12) is used, the error in the reconstructed charge falls to below 1%, while that in the phase falls to approximately 15 μrad (not shown). In addition, the ripple-like artefacts are absent.

4.4.2. Gaussian noise and regularisation strength

The noise in an experimental phase image can depend on the camera used and on the acquisition method (*e.g.*, single *vs* multiple hologram acquisition). In the presence of noise, reconstruction without using a regularisator is found to result in a charge density distribution that can deviate greatly from the input. A 0th order Tikhonov regularisator was therefore used here. As discussed in Section 4.1, the regularisation strength, which is defined by the value of λ, determines the ratio between the residual norm vector (the first term on the right of Eq. (14)) and the regularisation term. If $\lambda \to 0$, then the regularisation term vanishes and the cost function only relies on the residual norm vector, resulting in high frequency noise in the reconstructed charge density distribution. In contrast, if $\lambda \to \infty$ then the cost function favours the regularisation term and the reconstructed result diverges from the experimental data. A good choice for the regularisation parameter corresponds to an optimal balance between compliance with the

nd
ows
sidual
s of the
as gener-
with a re-
host-vertical
reconstructed
perturbations,
sing values of λ
ng smoothed out.
the plot, where the
represents a balance
nd smoothness of the
nt example, the optimal
nately 5, resulting in the

reconstructed charge density distribution shown in Fig. 15. At the edge of the mask, the reconstructed charge density deviates by 50% from the input distribution, while elsewhere the error is below 5%. The corresponding phase error is below 1%. Fig. 16 shows the influence on the reconstructed charge density distribution of using regularisation parameters of 0.5 and 50. For $\lambda = 50$, the charge distribution is too smooth, whereas for $\lambda = 0.5$ it is too noisy. It should be noted that the algorithm is designed to be insensitive to the presence of an arbitrary phase offset and an arbitrary phase ramp. Care in the interpretation of the result is therefore required if a real phase ramp may be present across the FOV.

4.4.3. *Confidence mask*

Experimental phase images can contain artefacts that originate from the specimen (*e.g.*, unwanted effects of dynamical diffraction, contamination or electron-beam-induced charging), from the microscope (*e.g.*, image distortions, or instabilities), from the detector (*e.g.*, undersampling or dead pixels), or from image analysis (*e.g.*, imperfect

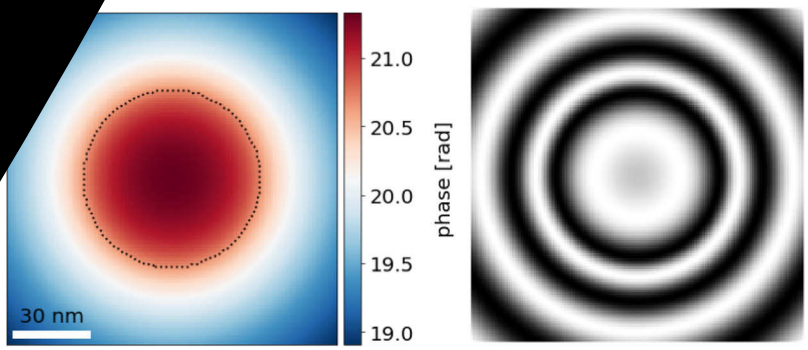

phase image (left) and corresponding 8-times-amplified contour map (right) for the charge density distribution shown in Fig. 11. The phase
$\frac{2\pi}{8}$ radians.

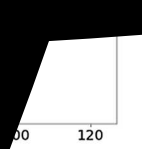

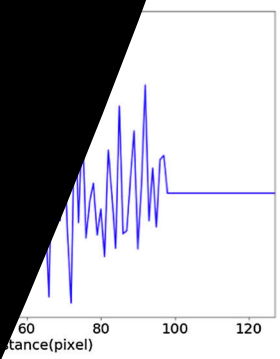

profiles across the centre ($x = 0$) are shown on the right. In each case, 1000 iterations of the reconstruction algorithm were used.

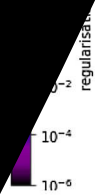

cted charge density
ptimal regularisation

magnification, position or
or example, it may not be
the phase everywhere across
ges in electron-beam-induced
se reasons, a confidence mask is
e signal in each pixel in the phase
re trustworthy are assigned a value
ssigned smaller values.
orm for the cost calculation of the re-
atrix $\mathbf{S}_e^{-1}$ is diagonal, with each entry on
o a single pixel in each phase image. These
ntries of the confidence matrix. If the con-
zero, then the corresponding residual does not
unction. The weighted norm therefore takes the

the result of a reconstruction performed after as-
f the pixels in the charged region (*i.e.*, inside the
are untrustworthy. The reconstructed projected charge

density distribution is then determined only from the phase outside the charged sphere and can be seen to deviate significantly from the input charge density distribution. Interestingly, although the charge density distribution cannot be reconstructed reliably, the retrieved phase outside the charged sphere is consistent with the input phase, suggesting that the projected electric field can also be retrieved correctly outside the sphere. This is not surprising, since the algorithm always delivers a unique solution (in a mathematical sense) for a given type and strength of regularisation. However, without information about the phase in the interior of the object, reconstruction of the charge density inside it cannot be unique. For example, for a metallic ellipsoid the charge on the surface produces the same electric field distribution outside the object as a line of constant charge density located on its axis [22]. This statement is also consistent with the general property of a homogeneous Laplace equation that the values in the domain volume depend solely on the values or their derivatives on the domain boundary. The possibility of being able to reconstruct the potential and electric field outside a specimen without needing to make use of phase information inside it has significant implications for applications such as the characterisation of electrically biased needle-shaped specimens for atom probe tomography, for which the electric field outside the specimen rather than the charge density inside it may be the parameter of primary interest for providing experimental input for the simulation of ion trajectories. Nevertheless, whereas techniques based on differential phase contrast can be used to record the projected electric field directly, an argument in favour of reconstructing the charge density from an off-axis electron hologram before then using it to infer the projected electric field is that the charge density is localised within the specimen, rather than extending outside the FOV.

4.4.4. Charges outside the field of view

As a result of the limited lateral extent of a phase image, it is often not possible to include all of the specimen or all of the phase change associated with the charge density distribution inside the FOV. This problem is particularly apparent when examining electrically-biased needle-shaped specimens, such as atom probe tomography needles or field emitters. It is illustrated for a uniform shell-like charge density distribution in Fig. 18. The phase of the entire shell (not shown) is calculated using the charge density shown in Fig. 18a. However, only

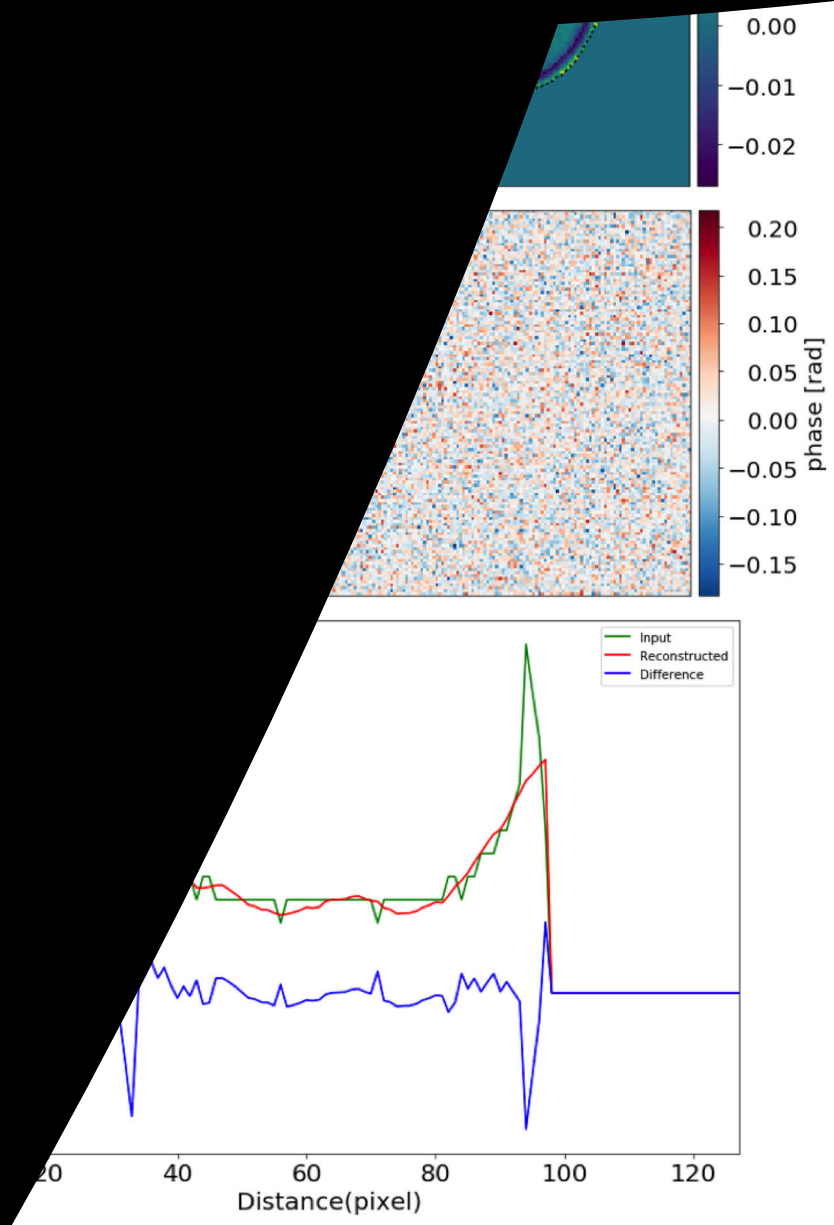

ase image shown in Fig. 12 with Gaussian noise of 0.05 rad added, for a regularisation parameter λ of 5, showing the tribution and its deviation from the input charge density (upper row, shown in units of e/pixel), the reconstructed phase iddle row), and the charge profile across the centre of the image ($x = 0$) extracted from the reconstructed (red) and input ifference (blue) (lower row).

age was used for the reconstruction. The ge density distribution, which is shown in antly from the input charge density, as the harges are present only in the masked region, e the FOV also contribute to the phase. Since the not include any boundary conditions, with the charges, the presence of charges outside the FOV by making use of additional buffer pixels, which are he edge of the FOV. These buffer pixels can be used to introduce a distribution of additional charge density around the edge of the image, in order to take into account the influence of unknown charges outside the FOV. They are only used during the reconstruction and are discarded when displaying the final reconstructed charge density inside the part of the specimen that is within the FOV. In the present example, Fig. 18c shows that the reconstructed result is almost consistent with the original input charge density when 8 buffer pixels are used at the border of the image.

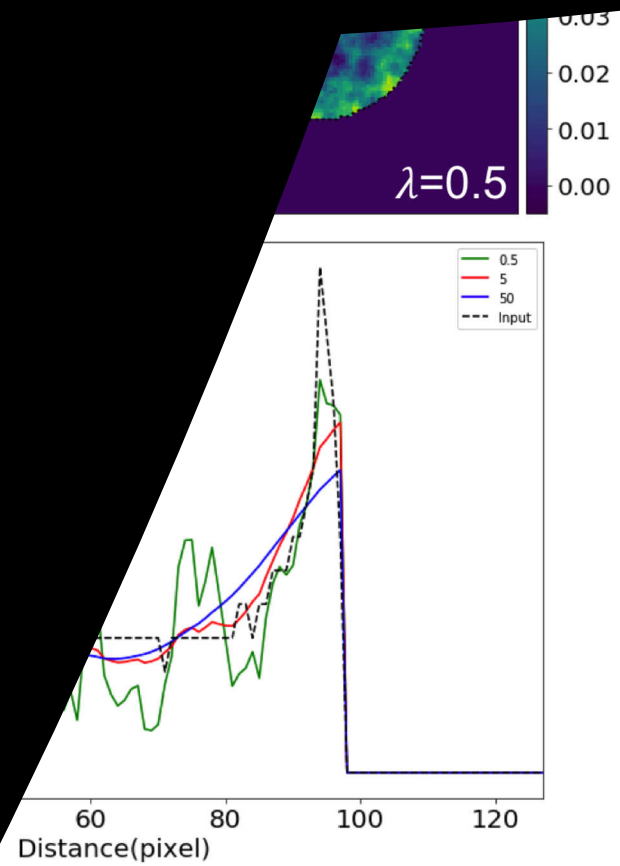

ty distributions starting from the phase image shown in Fig. 12 for regularisation parameters λ of
el shows the charge profiles across the centre for the input charge distribution (black) and the
ion parameters: 0.5 (green), 5 (red), and 50 (blue).

RW can affect the
erence wave that is
urbed significantly by
etic) fields, which may
nfluence of the PRW can
e density by implementing
chematic illustration of the
image is shown in Fig. 19 for
oint charge within the FOV. In
e tail of the electric field arising
vacuum reference wave, the mea-
s the projected potential of the po-
nmetrical with respect to its position.
n the vacuum reference wave originates
c field of the point charge, which decays
y the solid red line in Fig. 19. The measured
nce between the projected potential of the
and the projected potential in the vacuum re-
The red dashed line in Fig. 19 represents the po-
n reference wave region, which has to be added to
n the FOV with a negative sign to take the PRW into
ulting phase image is asymmetrical with respect to the

position of the charge. The red dashed line can be described as originating from a negative (virtual) point charge located on the other side of the biprism, as shown by a solid blue line in Fig. 19. The influence of the PRW can therefore be described by a region of virtual charges of opposite sign (mirror charges) that are located on the opposite side of the biprism at a distance that is equal to the interference distance. It can be treated in the same way as any other source of charge located outside the FOV, as described in Section 4.4.4, or alternatively by using a modified kernel that includes the PRW effect.

4.4.6. *Reconstruction from an experimental phase image*

A phase image recorded from a LaB_6 needle-shaped specimen that was electrically biased *in situ* in the TEM using an applied voltage of 50 V (Fig. 6c), from which the MIP contribution to the phase had been removed using the procedure describe above, was used for reconstruction of the charge density. The positions of image point charges in the forward model were calculated by assuming a distance between the needle and the contour-electrode of approximately 6 µm. The sampling density was 7 nm/pixel. A 4-pixel-wide buffer was also defined around the border of the image, in order to compensate for the presence of charges at unknown positions outside the FOV, as well as the presence of the PRW, as described in Sections 4.4.4 and 4.4.5. 0th order Tikhonov regularisation was used. An optimal value for the

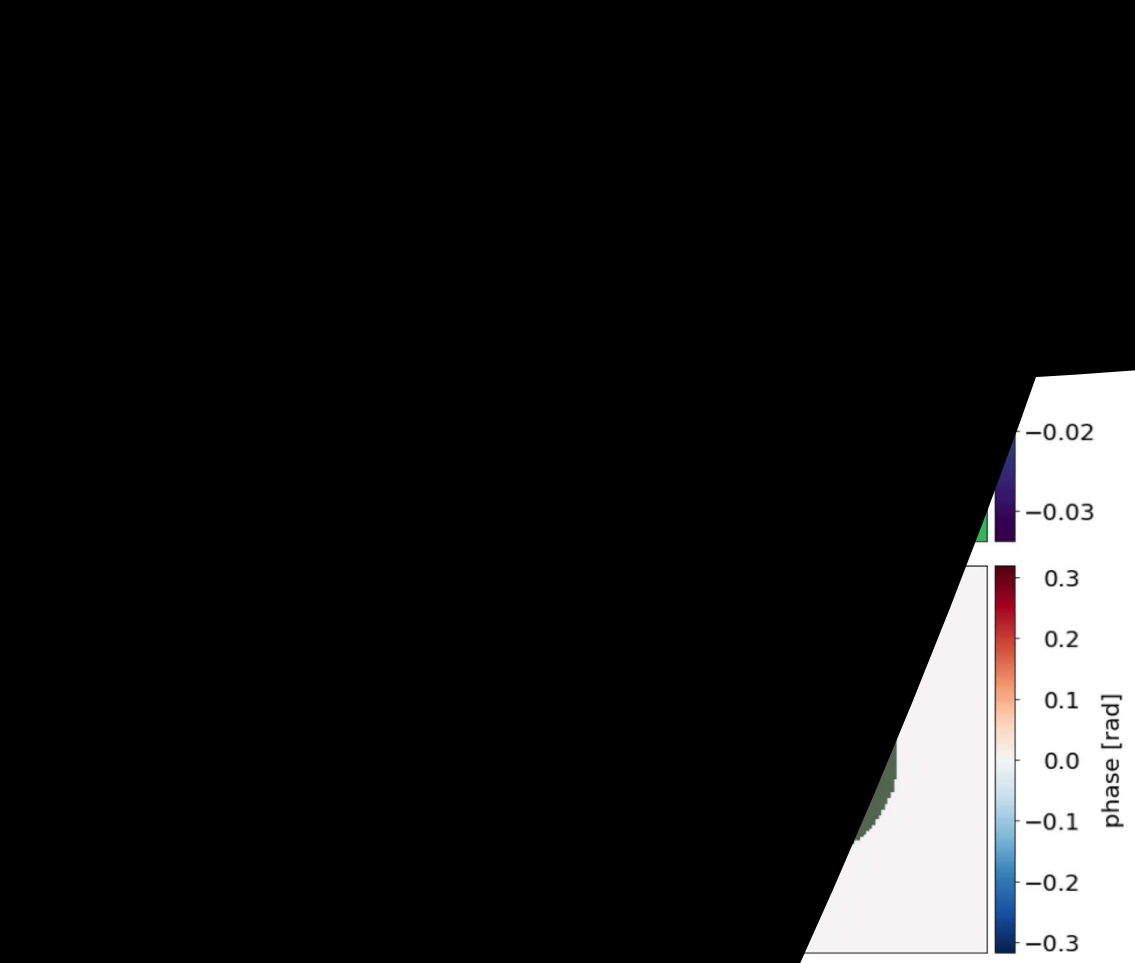

and its deviation from the input charge density (right), shown in units of e/pixel. The lower row shows the phase determined from the reconstructed charge density (left) and its deviation from the phase calculated from the input charge distribution (right).

original experimental image (see Fig. 20c and d), this discrepancy is at a level of below 1% and may result from a slight error in the selection of the mask, or from the finite sampling of the phase at the narrow apex of the needle. If the reconstructed charge density distribution obtained using the MBIR algorithm (Fig. 20) is compared with that obtained from the Laplacian of the phase (Fig. 7), it is clear that the noise in the fitted charge distribution is greatly reduced, as a result of the use of *a priori* knowledge (in particular, the mask and the regularisation parameter) when performing the reconstruction. Nevertheless, it should be noted that the result depends strongly on the values of several input parameters, which should be chosen carefully when applying the MBIR approach.

4.5. Reconstruction of charge density in three dimensions

Three-dimensional charge density distributions can in principle be

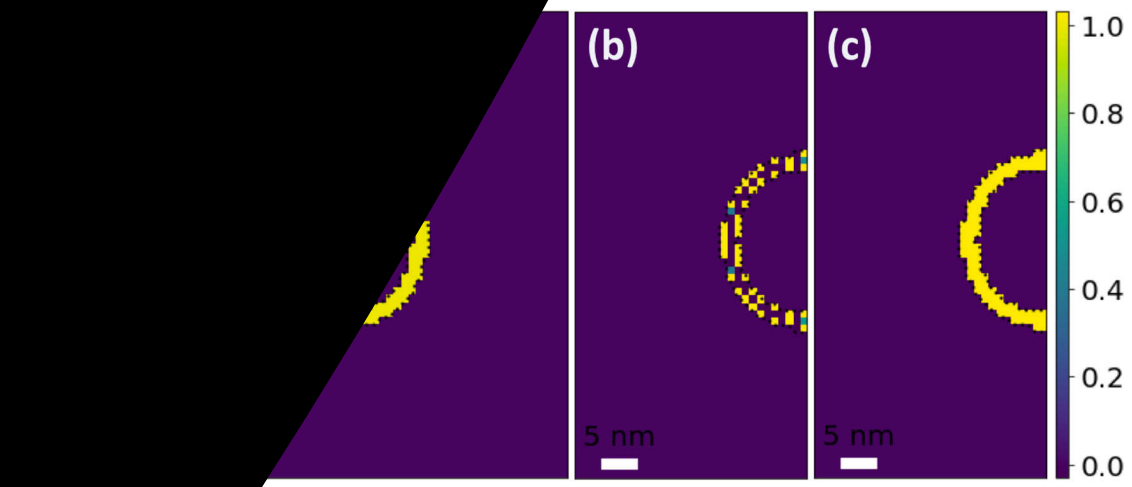

Fig. 18. Illustration of the reconstruction of only part of a charge density distribution to highlight the influence of the presence of charges outside the FOV. (a) shows a uniform shell-like charge distribution, which was used to generate a phase image. (b) and (c) show reconstructed charge distributions generated from only the left half of the phase image. (b) was generated without using any boundary pixels. (c) was generated by allowing additional charge density to be fitted in an additional boundary region that had a width of 8 pixels just outside the right edge of the image. The boundary pixels were then removed to display the final fitted charge density within the original FOV. All of the images are shown in units of e/pixel.

rad was added to each
s. The tilt angle range was chosen to be ± 50°
s range can be achieved experimentally. The an-
hosen to be 10°, resulting in an input dataset to the
11 phase images in total. Three different three-di-
were used: the shell, the outer surface of the sphere
e-dimensional volume. 0th order Tikhonov regular-
l, as described in Section 4.3. The regularisation para-
t to be 100 for all three cases.

nd 22 show two-dimensional slices and line profiles
reconstructed three-dimensional charge density. As ex-
use of a shell mask, which defines the true positions of the
elivers the best results. If only the outer surface of the sphere
as a mask, then the algorithm retrieves the key feature of the
distribution (the homogeneous surface charge) correctly. How-
he reconstructed charge is smoothed slightly into the volume of
here and exhibits small oscillations next to the shell region. If the
three-dimensional volume is used, then the basic features of the
rge density are reproduced (see Fig. 22), but additional spreading of
e charge and high frequency artefacts are present across the FOV.
Although further tests are required to optimise the use of the MBIR
approach for three-dimensional charge density reconstruction, the re-
sults presented here are highly encouraging.

5. Summary and conclusions

Three different approaches have been described for the measure-
ment of charge density distributions in nanoscale materials from elec-
tron optical phase images recorded using off-axis electron holography:

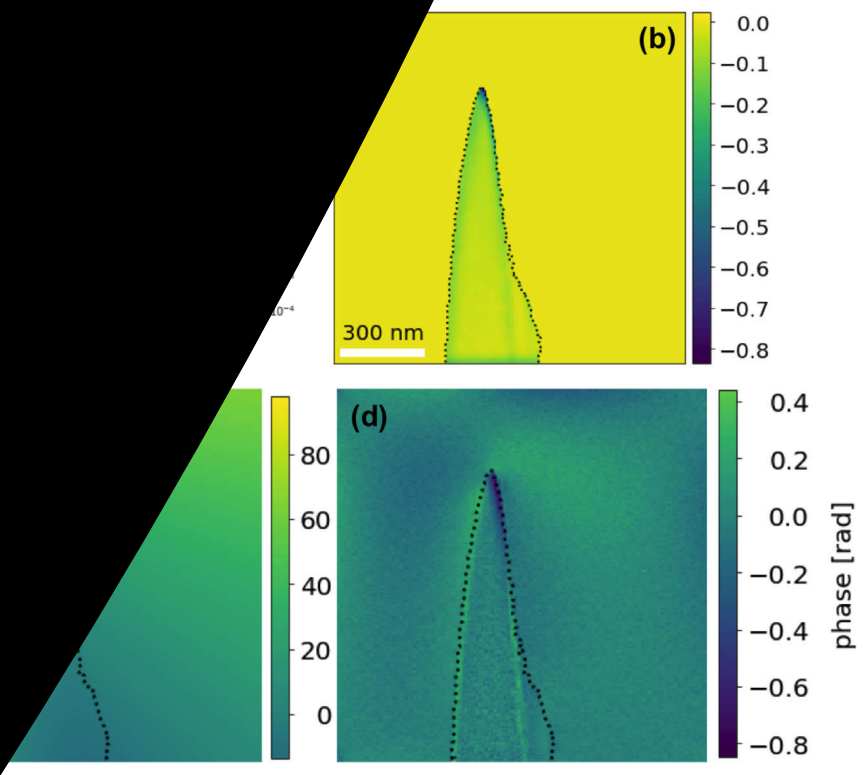

Fig. 20. Reconstruction of the projected charge density distribution from an experimental phase image of a needle-shaped LaB_6 specimen that was electrically biased *in situ* in the TEM at 50 V, from which the MIP contribution to the phase had been subtracted (Fig. 6c), using 0th order Tikhonov regularisation. (a) Application of L-curve analysis to determine that the optimal value of the regularisation parameter λ is 10. (b) Reconstructed projected charge density distribution, shown in units of e/pixel. (c) Phase image determined from the reconstructed projected charge density. (d) Difference between the reconstructed phase shown in (c) and the experimental phase image shown in Fig. 6c. Note the different intensity scales in (c) and (d).

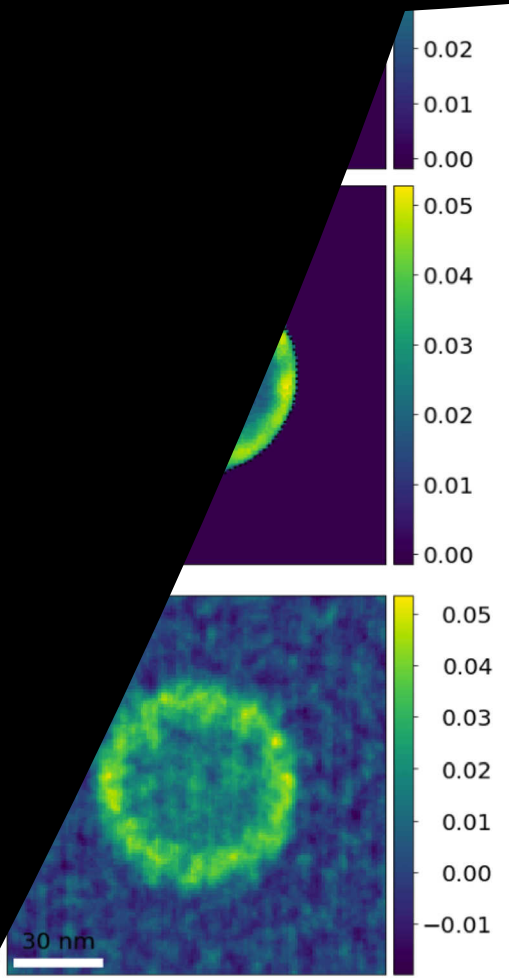

parameter λ is set to be 100 for all three cases. Different three-dimensional masks were used to define the possible locations of the reconstructed charge: the shell that defines the original charge distribution (upper row); the outer surface of the sphere (middle row); the full three-dimensional reconstruction volume (lower row). The left column shows the reconstructed charge distribution in the central slice ($z = 0$), while the right column shows the corresponding projected charge density distribution.

on 3.2), in which a
ge density and phase
on 3.1), which is based
a recorded phase image;
on approach (Section 4), in
odel used to simulate phase
experimental measurements is
nt approach (Section 3.2) relies
or the charge density and phase
ecimen geometry and requires the
wave to be included in the model.
n (Section 3.1) is the most direct and
ing the projected charge density dis-
e and is insensitive to the presence of a
nd charges outside the field of view. How-
ge density can be noisy (since the approach
of derivatives). In the MBIR approach (Section
l approximates each charged voxel as a homo-
sphere and a mirror charge. It can incorporate *a*
hrough the use of masks, regularisation parameters
cal constraints, resulting in lower noise but requiring care in the selection of parameters to avoid the introduction of artefacts. A further advantage is that boundary pixel regions can be used to take account of the presence of charges outside the field of view and the perturbed reference wave (Section 4.4.4). Artefacts can be tackled by assigning zero confidence to regions of phase images that contain untrustworthy information (Section 4.4.3). It is important to note that different charge distributions inside an object can result in the same electrostatic potential and phase distribution outside it.

The three approaches have been tested on an experimental phase image of an electrically biased needle-shaped LaB_6 specimen and have been shown to provide consistent results for the charge density. The phase shift of a line charge is used as a simple model in the analytical model-dependent approach. Projected charge density distributions retrieved using the model-independent approach (Fig. 7a and b) and the MBIR approach (Fig. 4.4.6) show that most of the charge is located close to the surface of the needle, with charge accumulation at its apex. The result obtained using the MBIR approach has much less noise than that obtained using the model-independent approach. Three-dimensional charge density distributions can in principle be reconstructed using each approach, either by applying a standard backprojection-based tomographic reconstruction algorithm to projected charge

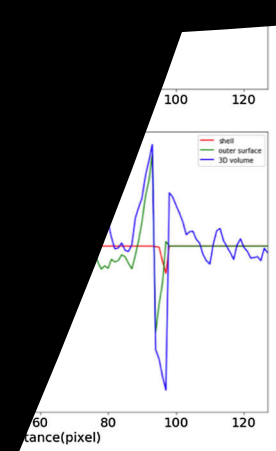

$z = 0$). The three line profiles correspond to reconstructions for: "3D volume" – no mask applied (blue), "outer surface" – mask includes the whole sphere (green), "shell" – mask includes only the shell of the sphere where the charge was placed (red).

…th for focused ion beam preparation of the LaB_6 specimen. This …oject was carried out within the framework of a scientific service …greement between the Ernst Ruska-Centre for Microscopy and Spectroscopy with Electrons in Forschungszentrum Jülich and Gatan Inc. The authors acknowledge the European Union for funding through the Marie Curie Initial Training Network SIMDALEE2 (Marie Curie Initial Training Network (ITN) Grant No. 606998 under FP7-PEOPLE-2013-ITN). V.M. thanks the Deutsche Forschungsgemeinschaft for funding within the framework of the SFB 917 project "Nanoswitches". R.D.-B. thanks the Deutsche Forschungsgemeinschaft for a Deutsch-Israelische Projektkooperation (DIP) Grant and the European Union's Horizon 2020 Research and Innovation Programme Q-SORT (Grant No. 766970 under H2020-FETOPEN-2016-2017). This project has received funding from the European Union's Horizon 2020 research and innovation programme under grant agreement No. 823717-ESTEEM3.

…radius R and charge q can be written in the form

$$\text{…} \geq R$$

$$\text{…}_1 < R \quad ,$$

$$\text{if } d_2 < R$$

$d_2 = \sqrt{(x - x_0')^2 + (y - y_0')^2}$ are the projected distances to the charge and its image charge, respectively, … the heights at which an electron enters the sphere and its image, respectively, and (x_0, y_0) and (x_0', y_0') are the …here and its image, respectively.

… Tunneling across a ferroelectric, Science 313 (5784)

…, H. Sasaki, T. Matsumoto, H. Sawada, Y. Kohno, S. Otomo, …imaging of built-in electric field at a pn junction by scanning …n microscopy, Sci. Rep. 5 (2015) 10040.

…ang, C.-Y. Wang, Y. He, K.L. Wang, C. Wang, D.J. Smith, … Direct mapping of charge distribution during lithiation of Ge …g off-axis electron holography, Nano Lett. 16 (6) (2016) 3748–3753.

[4] S. Katnagallu, M. Dagan, S. Parviainen, A. Nematollahi, B. Grabowski, P.A. Bagot, N. Rolland, J. Neugebauer, D. Raabe, F. Vurpillot, M.P. Moody, B. Gault, Impact of local electrostatic field rearrangement on field ionization, J. Phys. D: Appl. Phys. 51 (10) (2018) 105601.

[5] E. Völkl, L.F. Allard, D.C. Joy (Eds.), Introduction to Electron Holography, Springer Science & Business Media, 1999.

[6] H. Lichte, M. Lehmann, Electron holography—basics and applications, Rep. Prog. Phys. 71 (1) (2007) 016102.

[7] M. Lehmann, H. Lichte, Tutorial on off-axis electron holography, Microsc. Microanal. 8 (6) (2002) 447–466.

[8] G. Matteucci, G.F. Missiroli, G. Pozzi, Electron holography of long-range

…opy at atomic resolution, Nat. Phys. 8 (8) (2012) 611.
…el, S. Lahmann, U. Rossow, Composition dependence of po-
…AlInN/GaN quantum wells, Appl. Phys. Lett. 83 (6) (2003)

…de, M. Jetter, C. Wächter, T. Wunderer, F. Scholz, J. Zweck,
… contrast 2.0 – opening new “fields” for an established technique,
… 117 (2012) 7–14.
…Krause, A. Béché, M. Schowalter, V. Galioit, S. Löffler, J. Verbeeck,
…chattschneider, A. Rosenauer, Atomic electric fields revealed by a
…hanical approach to electron picodiffraction, Nat. Commun. 5 (2014)

… S.D. Findlay, T. Matsumoto, Y. Kohno, T. Seki, G. Sánchez-Santolino,
…, Direct visualization of local electromagnetic field structures by scanning
…ion electron microscopy, Acc. Chem. Res. 50 (7) (2017) 1502–1512.
…er-Caspary, F.F. Krause, T. Grieb, S. Löffler, M. Schowalter, A. Béché,
…oit, D. Marquardt, J. Zweck, P. Schattschneider, J. Verbeeck, R. Andreas,
…urement of atomic electric fields and charge densities from average mo-
…tum transfers using scanning transmission electron microscopy,
…ramicroscopy 178 (2017) 62–80.
…F. Missiroli, G. Pozzi, U. Valdre, Electron interferometry and interference electron
…icroscopy, J. Phys. E: Sci. Instrum. 14 (6) (1981) 649–671.
M. O’Keeffe, J. Spence, On the average Coulomb potential (Φ_0) and constraints on the electron density in crystals, Acta Crystallogr. Sect. A: Found. Crystallogr. 50 (1) (1994) 33–45.
…3] M. Beleggia, L.C. Gontard, R.E. Dunin-Borkowski, Local charge measurement using off-axis electron holography, J. Phys. D: Appl. Phys. 49 (29) (2016) 294003.
[44] F. Röder, A. Lubk, D. Wolf, T. Niermann, Noise estimation for off-axis electron holography, Ultramicroscopy 144 (2014) 32–42.
[45] E. Völkl, D. Tang, Approaching routine 2π/1000 phase resolution for off-axis type holography, Ultramicroscopy 110 (5) (2010) 447–459.
[46] E.G. Pogorelov, A.I. Zhbanov, Y.-C. Chang, Field enhancement factor and field emission from a hemi-ellipsoidal metallic needle, Ultramicroscopy 109 (4) (2009) 373–378.
[47] K. Svensson, Y. Jompol, H. Olin, E. Olsson, Compact design of a transmission electron microscope–scanning tunneling microscope holder with three-dimensional coarse motion, Rev. Sci. Instrum. 74 (11) (2003) 4945–4947.
[48] G. Singh, R. Bücker, G. Kassier, M. Barthelmess, F. Zheng, V. Migunov, M. Kruth, R.E. Dunin-Borkowski, S.T. Purcell, R.D. Miller, Fabrication and characterization of a focused ion beam milled lanthanum hexaboride based cold field electron emitter source, Appl. Phys. Lett. 113 (9) (2018) 093101.
[49] J. Caron, Model-based reconstruction of magnetisation distributions in nanostructures from electron optical phase images (Ph.D. thesis), Forschungszentrum Jülich, Zentralbibliothek, Jülich, 2017.
[50] A. Tarantola, Inverse Problem Theory and Methods for Model Parameter Estimation, Society for Industrial and Applied Mathematics, 2005.
[51] D.W. Kammler, A First Course in Fourier Analysis, Cambridge University Press, 2007.
[52] A.N. Tikhonov, V.I. Arsenin, Solutions of Ill-posed Problems, ser. Scripta Series in Mathematics, Winston and Distributed solely by Halsted Press, Washington and New York, 1977.
[53] J. Jackson, Classical Electrodynamics, Wiley, 2012.
[54] P.C. Hansen, Analysis of discrete ill-posed problems by means of the L-curve, SIAM Rev. 34 (4) (1992) 561–580.